Electronic Supporting Information to:

Nanoparticle anisotropy induces sphere-to-cylinder phase transition in block copolymer melts

Javier Diaz and Ignacio Pagonabarraga
CECAM EPFL

Marco Pinna and Andrei V. Zvelindovsky
University of Lincoln, UK

Keywords: block copolymer, nanoparticles, nanorod, colloid, hybrid material, nanocomposite

A. Details of the model

We present a mesoscopic model to simulate the dynamics of block copolymer nanocomposites with anisotropic NPs. This hybrid in-grid/out-of-grid dynamic algorithm combines a continuous description for the BCP with an individual description of NPs following Brownian dynamics.

The total free energy of the system can be decomposed as

$$F_{tot} = F_{pol} + F_{cpl} + F_{cc} \tag{1}$$

where the polymer free energy is F_{pol}, the coupling free energy F_{cpl} introduces the presence of the NPs in the BCP, and the colloid-colloid interaction is F_{cc}.

1. BCP modelling

The BCP is characterized by the order parameter $\psi(\mathbf{r},t)$ which is related to the differences in the local monomer concentration $\phi_A(\mathbf{r},t)$ and $\phi_B(\mathbf{r},t)$ of block A and B, respectively,

$$\psi(\mathbf{r},t) = \phi_A(\mathbf{r},t) - \phi_B(\mathbf{r},t) + (1-2f_0) \tag{2}$$

with the composition ratio $f_0 = N_A/(N_A+N_B)$ being the overall volume fraction of monomers A in the system. $\psi(\mathbf{r},t)$ is considered the local order parameter, which has a value 0 for the disordered-or homogeneous- state and $|\psi| > 0$ for microphase-separated regions.

The time evolution of $\psi(\mathbf{r},t)$ is dictated by the conservation of mass, resulting in the Cahn-Hilliard-Cook equation [1–3]

$$\frac{\partial\psi(\mathbf{r},t)}{\partial t} = M\nabla^2\left[\frac{\delta F_{tot}[\psi]}{\delta\psi}\right] + \eta(\mathbf{r},t) \tag{3}$$

with M being a mobility parameter and $\eta(\mathbf{r},t)$ being a gaussian noise parameter that satisfies the fluctuation-dissipation theorem

$$\langle\eta(\mathbf{r},t)\eta(\mathbf{r}',t')\rangle = -k_BTM\nabla^2\delta(\mathbf{r}-\mathbf{r}')\delta(t-t') \tag{4}$$

for which we have used the algorithm given by Ball[3]. k_BT sets the thermal energy scale of the diblock copolymer.

The polymeric free energy appearing in equation 1 is the standard Ohta-Kawasaki free energy[4], which can be further decomposed into short and long range terms $F_{pol} = F_{sr} + F_{lr}$ which can be expressed as

$$F_{\rm sr}[\psi] = \int d\mathbf{r}\left[H(\psi) + \frac{1}{2}D|\nabla\psi|^2\right] \tag{5a}$$

$$F_{lr}[\psi] = \frac{1}{2}B\int d\mathbf{r}\int d\mathbf{r}' G(\mathbf{r},\mathbf{r}')\psi(\mathbf{r})\psi(\mathbf{r}') \tag{5b}$$

with $G(\mathbf{r},\mathbf{r}')$ satisfying $\nabla^2 G(\mathbf{r},\mathbf{r}') = -\delta(\mathbf{r}-\mathbf{r}')$, i.e., the Green function for the Laplacian. The local free energy can be written as [5]

$$H(\psi) = \frac{1}{2}\tau'\psi^2 + \frac{1}{3}v(1-2f_0)\psi^3 + \frac{1}{4}u\psi^4 \tag{6}$$

where $\tau' = -\tau_0 + A(1-2f_0)^2$, u and v specify the order parameter bulk values [4]. The local free energy $H(\psi)$ possesses 2 minima values ψ_- and ψ_+ which are the values that $\psi(\mathbf{r},t)$ takes in the phase-separated domains. Parameter D in Equation 5a is related to the interface size $\xi = \sqrt{D/\tau'}$ between domains and B in Equation 5b to the periodicity of the system $H \propto 1/\sqrt{B}$ as the long ranged free energy takes into account the junction of the two chains in a diblock copolymer.

2. Modelling anisotropic nanoparticles

Nanoparticles are modelled as solid particles interacting with the BCP through a coupling term in the free energy

$$F_{cpl} = \sum_{p=1}^{N_p}\sigma\int d\mathbf{r}\ \psi_c(s(\mathbf{R}_p,\hat{\mathbf{u}}_p))\left[\psi(\mathbf{r})-\psi_0\right]^2 \tag{7}$$

where the position and orientation of particle p is specified by the vectors $\mathbf{R}_p$ and $\hat{\mathbf{u}}_p$ (which can be easily extended for biaxial particles). The parameter σ characterizes the interaction strength, while the chemical affinity ψ_0 is related to the coating in the surface of the particle. Tuning ψ_0 modifies the compatibility of the particle

with either phase of the BCP. Finally, the shape of the particle is introduced implicitly via the generalised radial distance $s(\mathbf{R}_p, \hat{\mathbf{u}}_p)$, while the dependence of the tagged function with s defines the core and corona of the NP. The functional form is chosen as[6]

$$\psi_c(s) = \exp\left[1 - \frac{1}{1-s}\right] \tag{8}$$

which is a continuously decaying function of s with continuous derivative on $\psi_c(1) = \psi_c'(1) = 0$, which allows for a natural definition of cut-off radius in the BCP-NP interaction. While for spherical particles the parametrisation is expressed as $s = (x^2+y^2+z^2)/R_{eff}^2$, for the case of anisotropic particles we choose to generalise the equation of a sphere into superellipses of arbitrary shape[7, 8]. The solid particle is enclosed by the surface

$$s = \left[\left|\frac{x}{a}\right|^{2n} + \left|\frac{y}{b}\right|^{2n} + \left|\frac{z}{c}\right|^{2n}\right]^{1/n} = 1 \tag{9}$$

for a resting super-ellipse with three main semi-axis a, b and c pointing into the X, Y and Z coordinates, respectively[9]. This family of surfaces enclose objects such as spheres, ellipsoids, prism and rounded-corner cuboids. The exponent n characterizes the family of shapes, while the relative values a, b and c determine the size and the anisotropy of the object. These parameters can be continuously tuned to model any shape belonging to the described set of surfaces. Euler angles α, β and γ are used within the algorithm to facilitate the calculation of forces and torques.

In order to model NPs at finite concentrations, we require an interparticle potential that prevents overlapping. The colloid-colloid potential contributes to the total free energy via the term

$$F_{cc} = \sum_{i \neq j} U(r_{ij}, \hat{\mathbf{r}}_{ij}, \hat{\mathbf{u}}_i, \hat{\mathbf{u}}_j) \tag{10}$$

which introduces a pairwise additive potential U depending in general on the distances and orientations of the pair particles. Oblate and prolate spheroid interactions have been modelled in the past using the Gay-Berne (GB) potential[10, 11] with notable results in the field of liquid crystals[12]. While this potential possess appropriate features -capturing the spheroid shape and possessing attractive and repulsive terms- we select a totally repulsive, Yukawa-like potential that allows for a larger time step. In order to capture the anisotropy of the particles, we substitute the Yukawa diameter for the orientational dependent $\sigma_{GB}(\hat{\mathbf{r}}_{ij}, \hat{\mathbf{u}}_i, \hat{\mathbf{u}}_j)$ parameter present in GB potentials, leading to a potential

$$U(r_{ij}, \hat{\mathbf{r}}_{ij}, \hat{\mathbf{u}}_i, \hat{\mathbf{u}}_j) = U_0 \left[\frac{\exp(r_{ij}/\sigma_{GB}(\hat{\mathbf{r}}_{ij}, \hat{\mathbf{u}}_i, \hat{\mathbf{u}}_j))}{r_{ij}/\sigma_{GB}(\hat{\mathbf{r}}_{ij}, \hat{\mathbf{u}}_i, \hat{\mathbf{u}}_j)} - 1\right] \tag{11}$$

which totally repulsive. At cut-off is introduced which depends on the colloid-colloid orientation with respect to each other, and the relative vector. This cut-off sets the range of the colloid-colloid interaction as $2a$, $2b$ and $2c$ along the three main axes of the colloid, that is, the cut-off conforms to the NP shape as specified in the coupling potential in equations 7, 8 and 9. Throughout this work, the colloid-colloid contribution plays a negligible role due to the highly diluted concentrations that are simulated.

3. Colloidal dynamics

Colloids undergo diffusive dynamics following the Langevin equation in the over-damped limit. The translational and orientational degrees of freedom of particle i evolve according to Brownian dynamics, respectively,

$$\frac{d\mathbf{R}_i}{dt} = \overleftrightarrow{M}_{trans}(\phi_i) \cdot \mathbf{f}_i + \xi_{trans} \tag{12a}$$

$$\frac{d\phi_i}{dt} = \overleftrightarrow{M}_{rot}(\phi_i) \cdot \mathbf{m}_i + \xi_{rot} \tag{12b}$$

where forces and torques are $\mathbf{f}_i$ and $\mathbf{m}_i$, respectively. The NP rotational state is specified by the three Euler angles contained in the angular vector $\phi_i = [\alpha_i, \beta_i, \gamma_i]$. The translational and rotational mobility tensor -$\overleftrightarrow{M}_{trans}$ and $\overleftrightarrow{M}_{rot}$,respectively- are rotated according to the orientation of the particle. The random translational and rotational vectors - ξ_{trans} and ξ_{rot}, respectively - satisfy the anisotropic fluctuation-dissipation theorem.

B. Computational details

In this work we make use of the Cell Dynamic Simulation (CDS) method to discretise the Cahn-Hilliard equation[13–15]. The CDS has been shown to allow for large time steps with a high degree of isotropy, which renders it appropriate for coarse-grained simulations. In this numerical method, the laplacian is discretised in a stencil as $\nabla^2\psi \approx \frac{1}{(\delta x)^2}[\langle\langle\psi\rangle\rangle - \psi]$. In three dimensions the local average value of a quantity ψ is expressed as

$$\langle\langle\psi\rangle\rangle = \frac{6}{80}\sum_{NN}\psi + \frac{3}{80}\sum_{NNN}\psi + \frac{1}{80}\sum_{NNNN}\psi \tag{13}$$

with NN, NNN, NNNN meaning nearest neighbours, next-nearest neighbours, and next-next-nearest neighbours, respectively. The colloidal dynamics is numerically solved using a standard forward Euler integration method.

1. Simulation parameters

In this section we provide details on some parameters which are not essential for the main text but are crucial for reproduciblity of the simulations.

The BCP parameters are set to standard values as $\tau_0 = 0.35, u = 0.5, v = 1.5,\ D = 1.0,\ B = 0.02, M = 1$. The colloid parameters as set to $\sigma = 1, k_BT = 0.05, U_0 = 10.0$.

The BCC-to-HEX phase transition in the neat BCP ($ie\ \phi_p = 0$) is identified at $f_0^{*BCC-HEX} = 0.4122$ for the set of parameters that are used in this work. The space discresitation (lattice spacing) is $\delta x = 1.0$ and the time discretisation is $\delta t = 0.1$. The system size in all simulations is $V = 64^2 \times 32$ grid points, expect for the large scale snapshots in figure 3 (c), (d) and (e) in the main text, where the number of grid points is $V = 128^2 \times 32$.

2. *Length scales*

To facilitate reproducibility we provide details on the length scales and relative length scales in the system. The interface thickness between the A and B interface can be analytically determined as $\xi_{interface} = \sqrt{D/\tau} = 1.69$ grid points. The BCP domain diameter (diameter of spheres in BCC and diameter of cylinders in HEX phase) is estimated from simulations as $R_\psi \approx 6.0$ grid points while the periodicity is found to be $H_{\psi-BCC} = 11.0$ and $H_{\psi-HEX} = 10.0$ grid points.

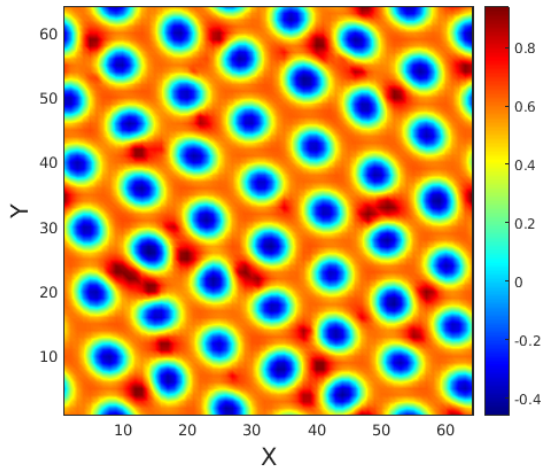

FIG. S1. Horizontal 2D slice of a NP anisotropy induced HEX cylindrical phase. This colourmap displays the values of ψ. Dark red areas indicate the placement of NEs.

3. *Minkowski functionals: the Euler characteristic χ_E*

The Minkowski functionals (MF) have been used to determine the details of the BCP phase transition. The MF provide useful information on the BCP geometry and topological structure: volume, surface, curvature and the Euler characteristic χ_E. All MFs are calculated for all simulations but χ_E is found to provide the most relevant information. We study the behaviours of these four numbers as function of time generating a black and white image from the density field of the matrix for every configuration generated by the CDS program. As in our previous papers, the implementation used here is adapted from the work of Blasquez and Poiraudeau[16]. In their publication and in particular in their eq.2 is also present a very small misprint.[16] We describe the image as a set of cubic voxels (set to 1 (black) for the image and 0 (white) for the background or for the seconf polymer). The Minkowski functionals have been calculated for the 3D discretized object in the following way: the volume (V = n_3), the surface area (S = -6n_3+ 2n_2), the mean curvature (2H = 3n_3 - 2n_2 + n_1), and the Euler characteristic (χ_E = -n_3 + n_2 - n_1 + n_0) where n_3 is the number of open cubes, n_2 the number of open faces, n_1 the number of open edges and n_0 the number of open vertices.[17, 18] Following the Ref.[16] for each black voxel we examine only the 13 neighbours called N_{ijk} where i, j, k indicate the position of the voxel in the box, and find the following contributions Δn_i for a black voxel N_{ijk}:

$$\begin{aligned}\Delta n_2 = 3 &+ Q(i,j,k-1) + Q(i,j-1,k) \\ &+ Q(i-1,j,k) \end{aligned} \tag{14}$$

$$\begin{aligned}\Delta n_1 = 3 &\\ &+ Q(i,j,k-1)\cdot Q(i,j-1,k)\cdot Q(i,j-1,k-1) \\ &+ Q(i,j,k-1)\cdot Q(i+1,j,k-1) \\ &+ Q(i,j,k-1)\cdot Q(i,j+1,k-1) \\ &+ Q(i,j,k-1)\cdot Q(i-1,j,k)\cdot Q(i-1,j,k-1) \\ &+ Q(i,j-1,k)\cdot Q(i+1,j-1,k) \\ &+ 2\cdot Q(i-1,j,k) \\ &+ Q(i-1,j-1,k)\cdot Q(i,j-1,k)\cdot Q(i-1,j,k) \\ &+ Q(i,j-1,k) \end{aligned} \tag{15}$$

$$\begin{aligned}\Delta n_0 = 1 &+ Q(i-1,j,k) \\ &+ Q(i,j-1,k)\cdot Q(i+1,j-1,k) \\ &+ Q(i-1,j-1,k)\cdot Q(i,j-1,k)\cdot Q(i-1,j,k) \\ &+ Q(i,j,k-1)\cdot Q(i+1,j,k-1)\cdot Q(i+1,j-1,k) \\ &\cdot\ Q(i,j+1,k-1) \\ &+ Q(i-1,j,k-1)\cdot Q(i,j,k-1)\cdot Q(i,j+1,k-1) \\ &\cdot\ Q(i-1,j+1,k-1)\cdot Q(i-1,j,k) \\ &+ Q(i,j-1,k-1)\cdot Q(i+1,j-1,k-1) \\ &\cdot\ Q(i+1,j,k-1)\cdot Q(i,j,k-1) \\ &\cdot\ Q(i,j-1,k)\cdot Q(i+1,j-1,k) \\ &+ Q(i-1,j-1,k-1)\cdot Q(i,j-1,k-1) \\ &\cdot\ Q(i,j,k-1)\cdot Q(i-1,j,k-1)\cdot Q(i-1,j-1,k) \\ &\cdot\ Q(i,j-1,k)\cdot Q(i-1,j,k) \end{aligned} \tag{16}$$

with Q(i,j,k)= 1-N_{ijk} where $N_{ijk} = 1$ for a black voxel (object) and $N_{ijk} = 0$ for a white voxel (background). The total numbers n_i are found by summation of Δn_i. The algorithm walks along the voxel grid exploring the

preceding neighbours: for the eqs: 14-16 we first run index k, then j and finally i.

4. *Auxiliary parameters*

The autocorrelation function is calculated as

$$C_{\hat{\mathbf{u}}}(t) = \frac{1}{N_p}\sum_{i=1}^{N_p}[\hat{\mathbf{u}}(t)\cdot\hat{\mathbf{u}}(0)]^2 \tag{17}$$

The time autocorrelation of the NP orientations can provide information regarding the dynamic orientational relaxation.

C. Kinetic pathway of composite system

Further details on the kinetic pathway of the three regimes (BCC spheres, COEXistence and HEXagonal cylinders) are found in figure S2. In a) we display a linear plot of χ_E in time, where the time scale of the HEX phase is found to be extremely small, compared to the rather slow COEX phase. The HEXagonal phase is greatly accelerated by the cooperative initial orientation of particles. NPs are breaking the symmetry at $t = 0$, which facilitates the formation of the uni-axial domains.

Nonetheless, it is important to notice that figure S8 shows that a random but coherent initial orientation does result in a similar χ_E profile with only a small variance, *ie*, the initial direction plays a sub-dominant in the HEX time scale.

The COEXistence phase in figure S2 a) is considerably slower than the other two phases. This can be explained as a consequence of the formation of grains with phase HEX (high local concentration) and BCC (low local concentration). In a slower time scale these grains grow in size (figure S3 and fig 3 c) in the main text).

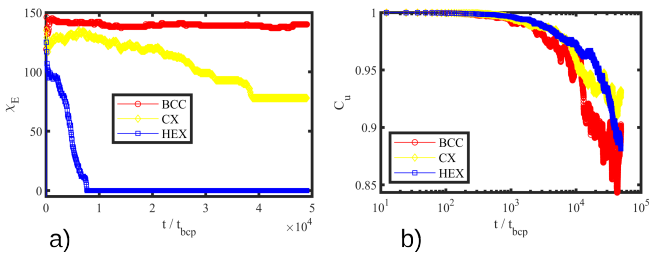

FIG. S2. a) Time evolution of the Euler characteristic χ_E for three representative regimes: BCC($\phi_p = 0.0016$), CX($\phi_p = 0.006$) and HEX($\phi_p = 0.0098$). The aspect ratio of the NE is $e = 1/8$, with all the parameters corresponding to figure 1 (a) in the main text. The χ_E curves are from a single simulation run. In b) the autocorrelation of particle orientation. Snapshots of the system are provided in figure S3.

D. Role of NE length and shape

In the main text, figure 3 (a) we use NEs with length $2a/H_0 = 1.44$, comparable with the BCP periodicity. The NE length $2a$ can be additionally compared with the shortest distance between BCP interfaces, $h = H_0 - R_\psi$, where the BCP sphere diameter is subtracted from the BCC periodicity. In figure S4 we explore the phase transition for shorter NEs with lengths $2a/H_0 = 0.72$ and $2a/H_0 = 0.36$, corresponding to $2a/h = 1.6$ and $2a/h = 0.8$, respectively. The NE aspect ratio is kept $e = 1/8$. The system volume is re-scaled accordingly as the BCP dimensions are increased. Comparing figure S4 with figure 3a in the main text, the transition can be seen to persist for $2a/H_0 = 0.72$, where the BCP transitions into $\chi_E \sim 0$ similarly as for longer NEs. Shorter NEs with $2a/H_0 = 0.36$ continue to induce a clear decrease in the number of BCP domains, into a more connected morphology, but its effect is less drastic and is considerably smoother. This can be attributed to the reduced impact of shorter NEs, as will be discussed in section G and figure S11. Figure S4 allows to characterise the reported transition as belonging to intermediately sized NEs with lengths $2a$ comparable or smaller with respect to the BCP periodicity. Larger NEs can be expected to introduce large distortions in the BCP mesophase directly via its inclusion in the system, as cannot be accommodated into the BCP structure. On the other hand, much shorter NEs can be expected to induce modifications in the BCP via its collective aggregation.

Equation 9 describes the generalised shape of a super-ellipse (ellipsoid, cuboid ...). In this work we have focused on the role of anisotropy of ellipsoids, as they allow for a well-defined repulsive interaction (based on the standard Gay-Berne potential) as well for the ability to recover the spherical shape in the case of aspect ratio $e = 1$. Nonetheless, the presented model allows to simulate NPs of generalised shape, in the absence of colloid-colloid interaction. Figure S5 shows that the phase transition mechanism is relatively generic, occurring for a variety of NP shapes. Even though the colloid-colloid interaction is not considered in these simulations, instances of overlapping can be considered negligible at such low concentrations. The persistence of the phase transition for generic NP shape suggests that the transition is generic and only requires highly anisotropic NPs to be triggered.

E. Further details on the discussion regarding equilibrium

We repeat the same simulation setup as in figure 1 in the main text, with a random initial orientation of each NPs, that is, the initial orientation of each NP is uncorrelated with the rest of the NPs. The NP position is similarly random, as in figure 1 in the main text. Figure S7 shows the Euler characteristic for a system of NSs and NEs with $e = 1/8$. A totally disordered initial distribu-

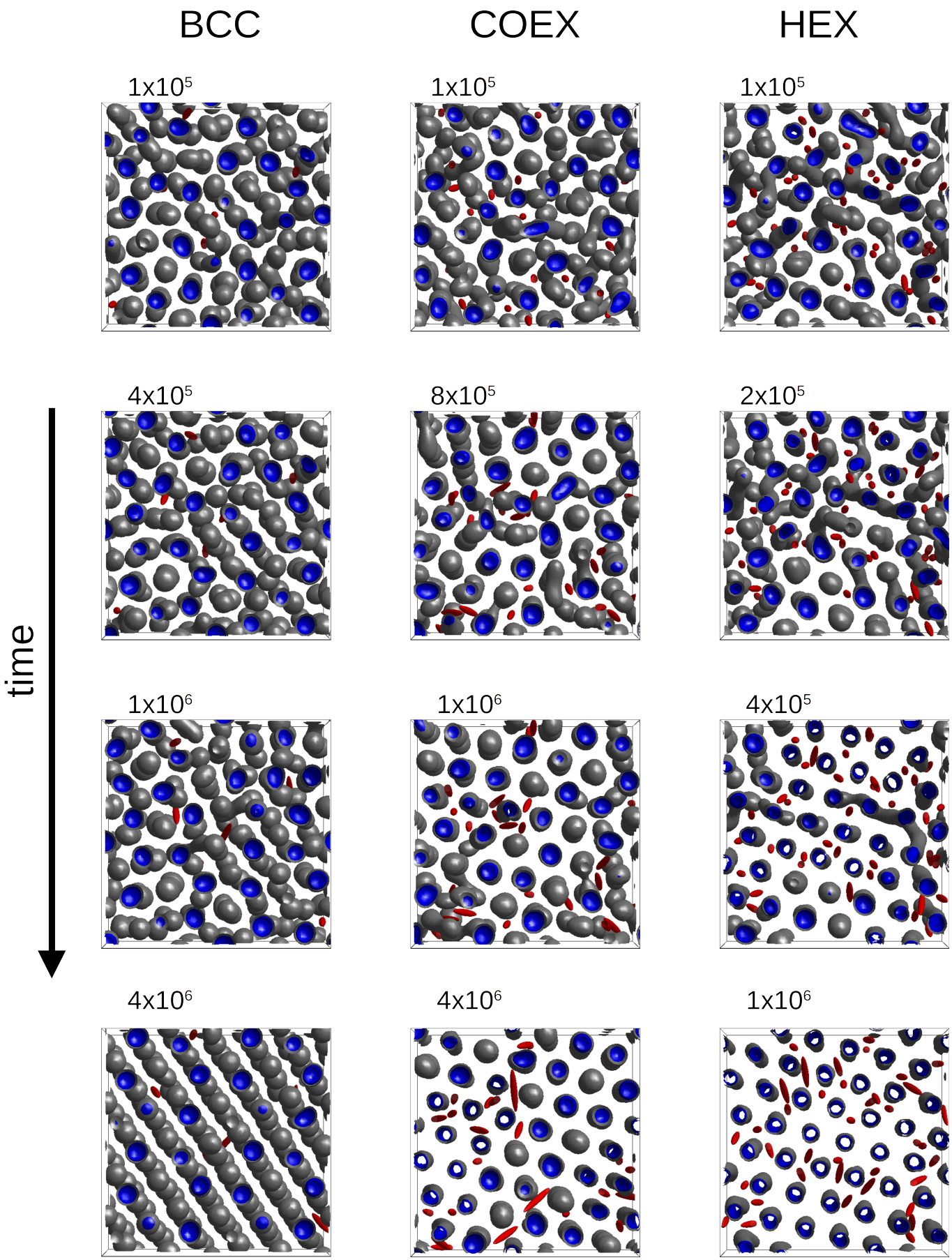

FIG. S3. Snapshots representatives of the three regimes: BCC($\phi_p = 0.0016$), CX($\phi_p = 0.006$) and HEX($\phi_p = 0.0098$). The time step is shown above each snapshot. The simulations correspond to the χ_E curve in figure S2.

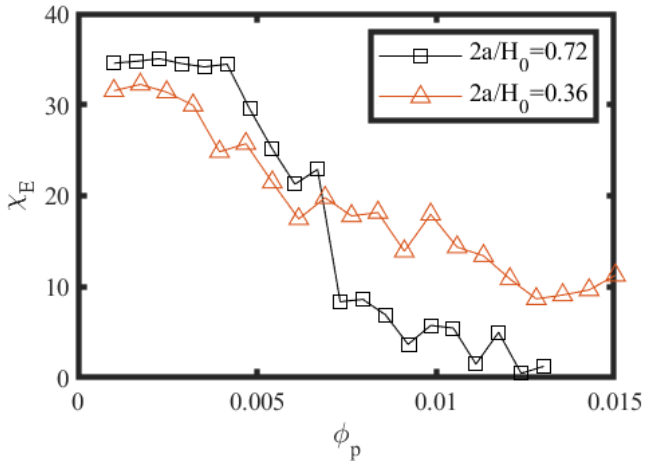

FIG. S4. BCC sphere to HEX cylinder phase transition induced by smaller NE length $2a/H_0 = 0.72$ and $2a/H_0 = 0.36$, characterised by the Euler characteristic χ_E, for a fixed aspect ratio $e = 1/8$. The system volume is re-scaled as the BCP dimensions are increased.

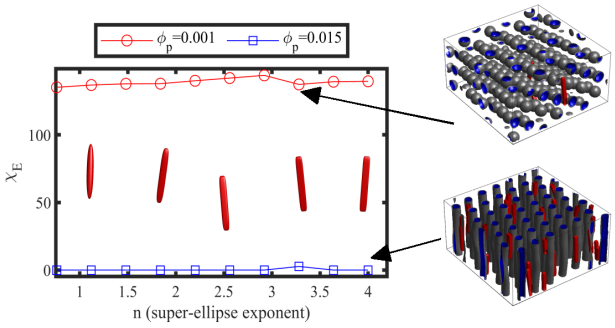

FIG. S5. Anisotropy-induced phase transition for several shapes beyond the spheroid used in the main text, for a fixed aspect ratio $e = 1/8$. Two volume fractions are considered below and above the critical one: $\phi_p = 0.01$ and $\phi_p = 0.015$, respectively. The shape of the NP is controlled by the super-ellipse exponent n, which isosurfaces are shown for relevant values of n, spanning from prolate ellipsoids to cuboids.

tion of orientations in figure S7 has shown that the morphology of the BCP is different depending on the aspect ratio of the NP, at the same NP loading. Nonetheless, the final state is clearly relatively disordered, without any clear global orientation. We can explain this as each NP is creating a local preferential direction for the BCP to orient. Reorienting all the different orientational grains into a global nematic-like order requires to overcome several local energetic barriers to reorient each orientation domain. For this reason, it would require an excessive computational time to achieve a global orientation. Setting an initial coherent nematic-like orientation of NPs can help achieve the global ordering in a shorter time scale.

In figure S8 we perform 15 simulations where the global orientation of all NPs is random but coherent, that is, in

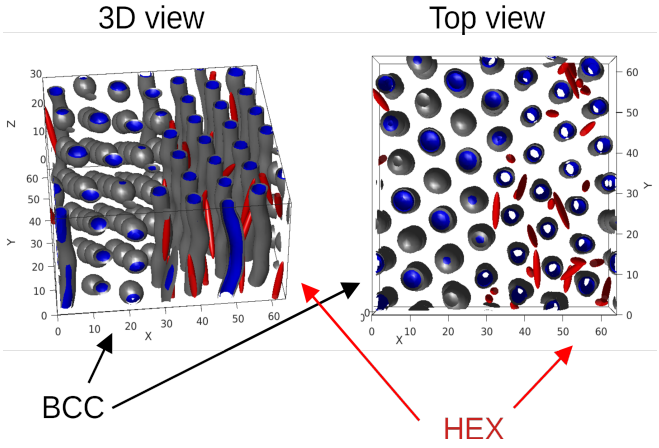

FIG. S6. 3D and top view of the coexistence of BCC and HEX phase in a moderate concentration $\phi_p = 0.01$ of NEs with aspect ratio $e = 1/8$. The NPs are initially segregated into the right half of the system, which evolves into the HEX phase, while the left half (devoid of NPs) maintains the BCC phase.

each simulation every NP has the same orientation. To clarify, the difference with figure S7 is that in this set the orientation of all NPs is equal but random at $t = 0$, for each simulation run. Figure S8 we show the cloud of points corresponding to the value of χ_E over time for each simulation run. Additionally, we show the averaged $< \chi_E >$ over all simulations. This provides information regarding the variability depending on the choice of initial orientation, suggesting that there is nothing extremely particular about the Z axis in the simulations of the main text. Instead, the equilibrated $\chi_E \sim 0$ value is reached at in a similar time scale, regardless of the initial orientation. Contrasting figure S7 and S8 the main conclusion one can obtain is that the energetic cost associated with obtaining a global coherent orientation is considerably high. By initially aligning all NPs along a particular direction (main text and figure S8) we can obtain the equilibrium morphologies in an accessible time scale. The problem of obtaining globally ordered BCPs is ubiquitous in experiments and simulations. To this end, external fields have been widely used.

The existence of a coexistence phase, as well as the highly metastability of block copolymer melts suggests the possibility of a memory effect on the transition that is described in this work. The hysteresis-like curve in figure S9 shows the same χ_E vs ϕ_p as in figure 3a in the main text, but considering two distinct initial BCP conditions: *cylinders to spheres*, by employing a cylindrical phase as the initial condition and reducing the concentration of particles in each simulation (this simulations are essentially a restart of both the colloidal and polymeric state of cylindrical phase simulation in figure 3a in the main text), and *spheres to cylinders* by restarting a BCC simulation with randomly placed NEs. The system is immediately subjected to a small annealing pe-

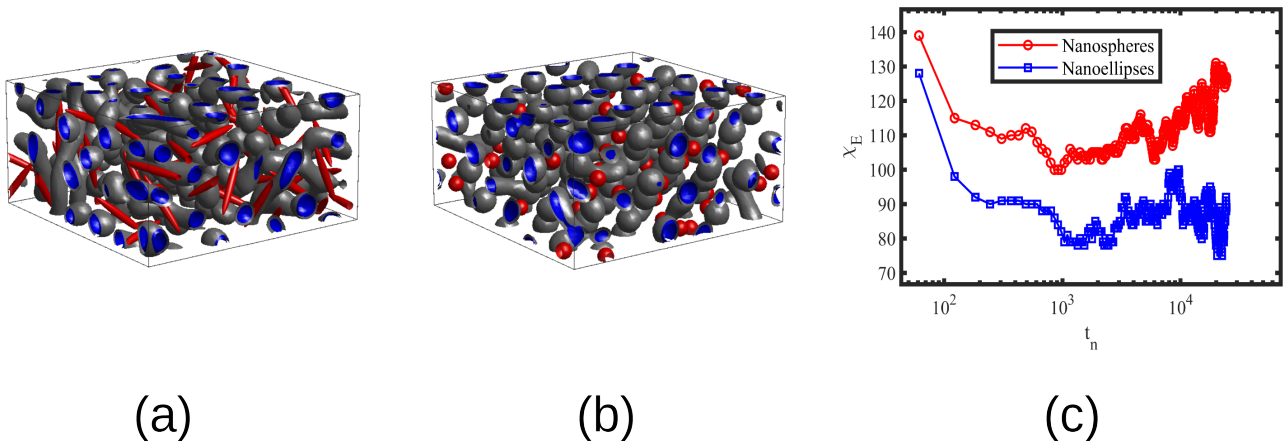

FIG. S7. Euler characteristic time evolution for nanoellipses and nanospheres, with an initially disordered configuration for the NPs. All the parameters are the same as in figure 1 in the main text.

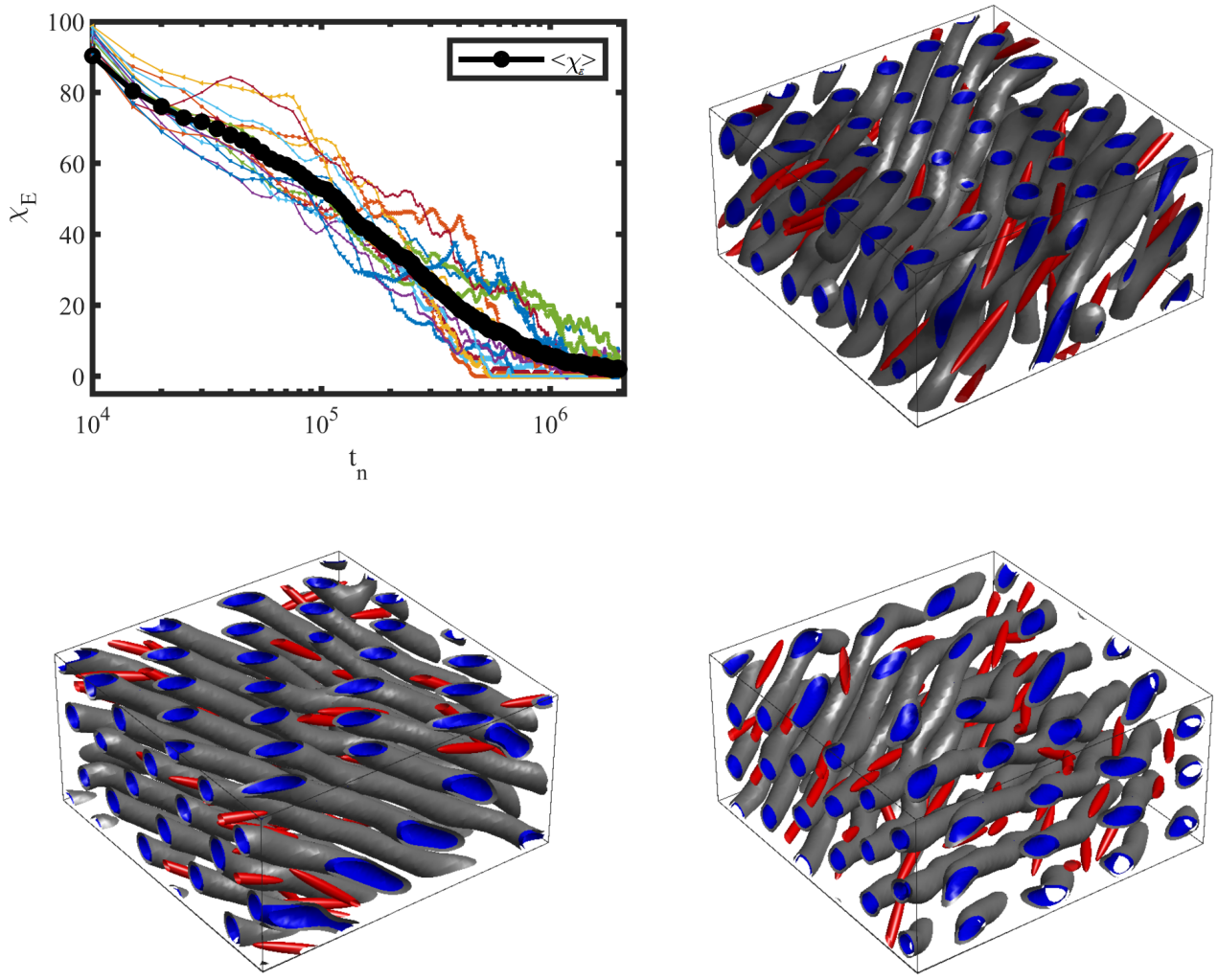

FIG. S8. Euler characteristic χ_E shown for 15 different simulation runs. For each simulation the orientation of all NPs is set to a single direction. In a thick line we show the averaged value of χ_E over all the independent runs. 3 random initial orientations are shown as examples of the final snapshot.

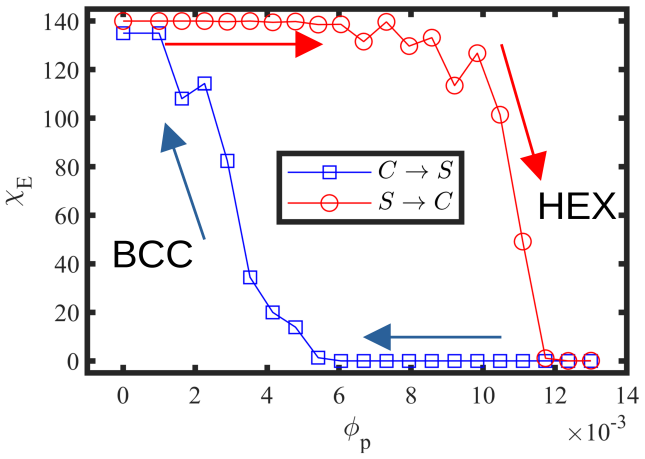

FIG. S9. Effect of the initial condition in the $\chi_E - \phi_p$ curve (same parameters as in figure 3a in the main text). Two distinct initial conditions are chosen: $S \rightarrow C$ the BCP is initialised as a BCC sphere phase and particles are randomly placed. For the $C \rightarrow S$ the BCP is initialised as HEX cylinders. The red/blue arrows indicate the process of adding/removing NPs from the system at $t = 0$. A moderate annealing period is used to facilitate the equilibration of the system.

riod during 5×10^4 steps for the system to equilibrate: a moderate noise $\eta_{noise} = 0.1$ is introduced in the Cahn-Hilliard-Cook equation following the work by Ball *et al* [3]. After relaxation the system clearly conserves memory of the initial condition, with a histeresis-like loop with a distinct pathway depending on the initial condition, which is different from the initially-disordered curve in figure 3a. The placement of the critical concentrations are shifted, depending on the initial condition of the BCP, which suggests the memory of the system with respect to the initial condition.

F. Phase transition driven by minority-compatible ellipsoids

While this work is devoted to phase transitions induced by anisotropic majority-compatible NPs, minority compatible additives have been widely shown to induce BCP phase transitions, due to their ability to modify the effective composition of the system, *ie*, to increase the overall concentration of their hosting BCP phase. In fact, majority-compatible NPs are used throughout this work to be able to avoid other known BCP transition mechanism to mask the role of anisotropy.

In this section we study the effect of minority-compatible NPs within BCP domains. Figure S10 (a) shows the effect of a concentration ϕ_p of NEs in a similar setup as figure 3 (a) in the main text. While the reduction of the initial value of χ_E is consistent with figure 3 (a), the mechanism behind it is considerably different: Even at very low concentrations, minority-compatible NEs are reducing the value of χ_E, displaying no critical value before which χ_E is constant. Contrary to that, as more NEs are added into the system, more spherical domains are disturbed into elongated domains due to the inclusion of anisotropic NPs. This is in sharp contrast with the mechanism described in the main text. Here, the change in χ_E is gradual and due to the size of the NP, not exclusively due to the NP shape. Moreover, an effective BCP composition can be defined[19] as $f_{eff} = \phi_p + (1 - \phi_p) f_0$ which captures the growth of the hosting BCP phase. Comparing the pure BCP critical composition $f_0^{BCC-HEX} \approx 0.41$ in figure S10 (b), we can observe that the effective BCP composition in (a) remains below the critical value. This concludes that the transition shown in (a) is primarily due to the large size of the NP, and not to the shape (as opposed to the main text) or the volume fraction (as shown in previus works with isotropic small NPs [19]).

The phase diagram in figure S10 (b) can be compared with figure 5 in the main text showing an enhanced coexistence region, but a reduced effect in the BCC-HEX transition, which only occurs for $f \sim 0.41$, near the neat BCP transition.

G. Discussion on the origins of the phase transition

As discussed in the main text, the origin of the anisotropy-driven phase transition can be traced back to the distortion introduced by the NE shape, which is enhanced in the weak segregation regime of the BCP, and which introduces a preferential direction via ψ_c when the NP is non-spherical. Exploring the role of the segregation regime via χN involves spanning over several BCP phases, unless the symmetric BCP is chosen, in which the BCP morphology remains lamellar regardless of the segregation regime, above the order-disorder transition[20]. Therefore, in figure S11 (a), the coupling free energy is shown as a function of the Flory-Huggins parameter χN for a symmetric BCP $f_0 = 0.5$. After relaxation, F_{cpl} is averaged over time for different values of parameter B (see equation 5b), controls the degree of segregation N. The overall value of F_{cpl} decreases rapidly with the segregation regime, which results from the decrease in $(\psi - \psi_0)^2$ as the ψ profile reaches pure monomer-A and pure monomer-B concentrations in the bulk domains.

Furthermore, the coupling free energy can be shown to play a crucial role in the BCC-HEX phase transition. Figure S11 (b) shows the phase transition in terms of the scaling of the free energy σ, which sets the strength of the coupling free energy, for a volume fraction of NE $\phi_p = 0.015$, *ie* , above the critical volume fraction identified in figure 2 (a) in the main text. The Euler characteristic χ_E signals the transition from a BCC spherical morphology($\chi_E >> 1$) to a HEX cylindrical phase ($\chi_E \approx 0$), as the overall importance of the coupling free energy is increased with σ. We can identify an approximate critical coupling strength $\sigma^* \sim 0.25$. Additionally,

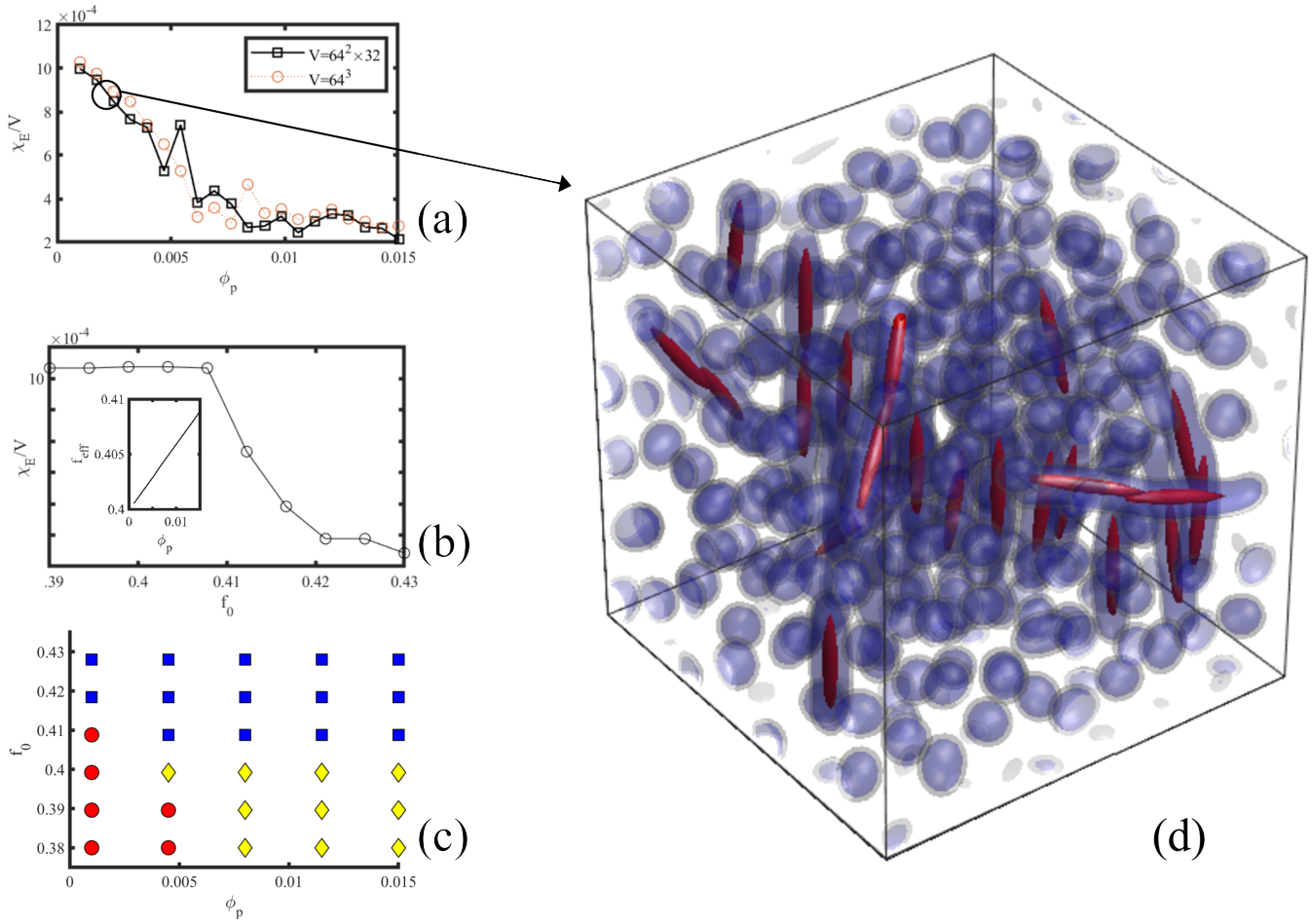

FIG. S10. Effect of minority-compatible ellipsoids ($e = 1/8$) in a BCC-forming BCP. In (a) the $\chi_E(\phi_p)$ curve is shown for a BCC-forming BCP with $f_0 = 0.4$, which can be compared with figure 3 (a) in the main text. Contrary to previous curves, the Euler characteristic χ_E is scaled with the system volume V to be able to compare different system sizes. In (b) the Euler characteristic for the neat BCP ($\phi_p = 0$) is shown for the transition in f_0, along with effective f_{eff} in the presence of a concentration ϕ_p of minority-compatible NPs. In (c) the phase diagram for $f_0 - \phi_p$ is shown, with red circles for BCC phase, blue squares for HEX cylinders and yellow diamonds for mixed states. A snapshot is shown in (d).

the free energy profile scaled with the coupling strength

$$F_{cpl}/\sigma = \int d\mathbf{r}\psi_c \left[\psi(\mathbf{r}) - \psi_0\right]^2 \tag{18}$$

is shown to decrease with σ, indicating that the bulk values in the percolating phase of the BCP profile are approaching the pure monomer concentration, *ie* , $\psi \to \psi_0$. Finally, a change in the scaling of $F_{cpl}/\sigma \propto \sigma^\nu$ is observed depending on the BCP phase. The change in the fitted exponent ν indicates that the distortion introduced by F_{cpl} is more easily alleviated in the HEX phase ($\chi_E \approx 0$, $\sigma > \sigma^*$) than in the BCC phase ($\chi_E >> 1$, $\sigma < \sigma^*$), as the quantity F_{cpl}/σ decreases more rapidly in the HEX ($\nu \approx -1$) than in the BCC phase ($\nu \approx -0.42$).

[1] Cahn, J. W. Free Energy of a Nonuniform System. II. Thermodynamic Basis. *The Journal of Chemical Physics* **1959**, *30*, 1121–1124.

[2] Cook, H. E. Brownian motion in spinodal decomposition. *Acta Metallurgica* **1970**, *18*, 297–306.

[3] Ball, R. C.; Essery, R. L. H. Spinodal decomposition and pattern formation near surfaces. *Journal of Physics: Condensed Matter* **1990**, *2*, 10303–10320.

[4] Ohta, T.; Kawasaki, K. Equilibrium morphology of block copolymer melts. **1986**, *19*, 12.

[5] Hamley, I. W. Cell dynamics simulations of block copolymers. *Macromolecular Theory and Simulations* **2000**, *9*, 363–380.

[6] Tanaka, H.; Araki, T. Simulation Method of Colloidal Suspensions with Hydrodynamic Interactions: Fluid Particle Dynamics. *Physical Review Letters* **2000**, *85*, 1338–

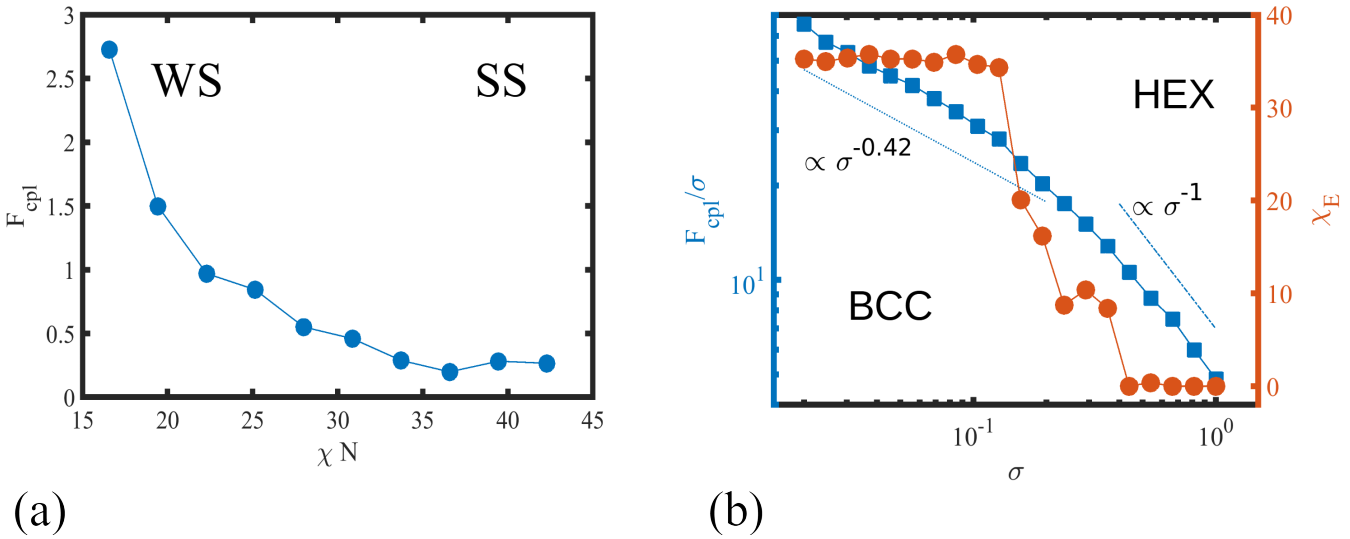

FIG. S11. (a) Coupling free energy for a symmetric BCP $f_0 = 0.5$ in the presence of a concentration $\phi_p = 0.01$ of NEs. (b) Phase transition in the BCP morphology in terms of the coupling strength σ for a volume fraction $\phi_p = 0.015$, using the logarithmic scale for all axes. In the left (blue square) the coupling free energy scaled with the coupling strength is plotted $F_{cpl}\sigma$. The scaling in the small and large σ limit is shown as dotted and dot-dashed lines, respectively, with an exponent σ^{ν} fitted numerically. In the right (red circles) the Euler characteristic is shown, indicating the BCP phase transition.

1341.

[7] Diaz, J.; Pinna, M.; Zvelindovsky, A. V.; Pagonabarraga, I. Nonspherical Nanoparticles in Block Copolymer Composites: Nanosquares, Nanorods, and Diamonds. *Macromolecules* **2019**, *52*, 8285–8294, Publisher: American Chemical Society.

[8] Diaz, J.; Pinna, M.; Zvelindovsky, A. V.; Pagonabarraga, I.; Shenhar, R. Block Copolymer–Nanorod Coassembly in Thin Films: Effects of Rod–Rod Interaction and Confinement. *Macromolecules* **2020**, Publisher: American Chemical Society.

[9] Donev, A.; Burton, J.; Stillinger, F. H.; Torquato, S. Tetratic order in the phase behavior of a hard-rectangle system. *Phys. Rev. B* **2006**, *73*, 054109.

[10] Gay, J. G.; Berne, B. J. Modification of the overlap potential to mimic a linear site–site potential. *The Journal of Chemical Physics* **1981**, *74*, 3316–3319.

[11] Berne, B. J.; Pechukas, P. Gaussian Model Potentials for Molecular Interactions. *J. Chem. Phys.* **1972**, *56*, 4213–4216.

[12] De Miguel, E.; Rull, L. F.; Chalam, M. K.; Gubbins, K. E. Liquid crystal phase diagram of the Gay-Berne fluid. *Molecular Physics* **1991**, *74*, 405–424.

[13] Oono, Y.; Puri, S. Study of phase-separation dynamics by use of cell dynamical systems. I. Modeling. *Physical Review A* **1988**, *38*, 434–453.

[14] Oono, Y.; Puri, S. Computationally efficient modeling of ordering of quenched phases. *Phys. Rev. Lett.* **1987**, *58*, 836–839.

[15] Puri, S.; Oono, Y. Study of phase-separation dynamics by use of cell dynamical systems. II. Two-dimensional demonstrations. *Phys. Rev. A* **1988**, *38*, 1542–1565.

[16] Blasquez, I.; Poiraudeau, J. F. Efficient processing of Minkowski functionals on a 3D binary image using binary decision diagrams. *Journal of WSG* **2003**, *11*.

[17] Pinna, M.; Zvelindovsky, A. V.; Todd, S.; Goldbeck-Wood, G. Cubic phases of block copolymers under shear and electric fields by cell dynamics simulation. I. Spherical phase. *The Journal of Chemical Physics* **2006**, *125*, 154905.

[18] Pinna, M.; Zvelindovsky, A. V. M.; Guo, X.; Stokes, C. L. Diblock copolymer sphere morphology in ultra thin films under shear. *Soft Matter* **2011**, *7*, 6991.

[19] Huh, J.; Ginzburg, V. V.; Balazs, A. C. Thermodynamic Behavior of Particle/Diblock Copolymer Mixtures: Simulation and Theory. *Macromolecules* **2000**, *33*, 8085–8096.

[20] Matsen, M. W.; Bates, F. S. Unifying Weak- and Strong-Segregation Block Copolymer Theories. *Macromolecules* **1996**, *29*, 1091–1098.